ERDC/GSL TR-23-18

Geotechnical and Structures Laboratory

US Army Corps of Engineers®
Engineer Research and Development Center

ERDC
ENGINEER RESEARCH & DEVELOPMENT CENTER

Residual Strength of a High-Strength Concrete Subjected to Triaxial Prestress

George H. Vankirk, Andreas O. Frank, Michael J. Roth, Brett A. Williams, and William F. Heard

December 2023

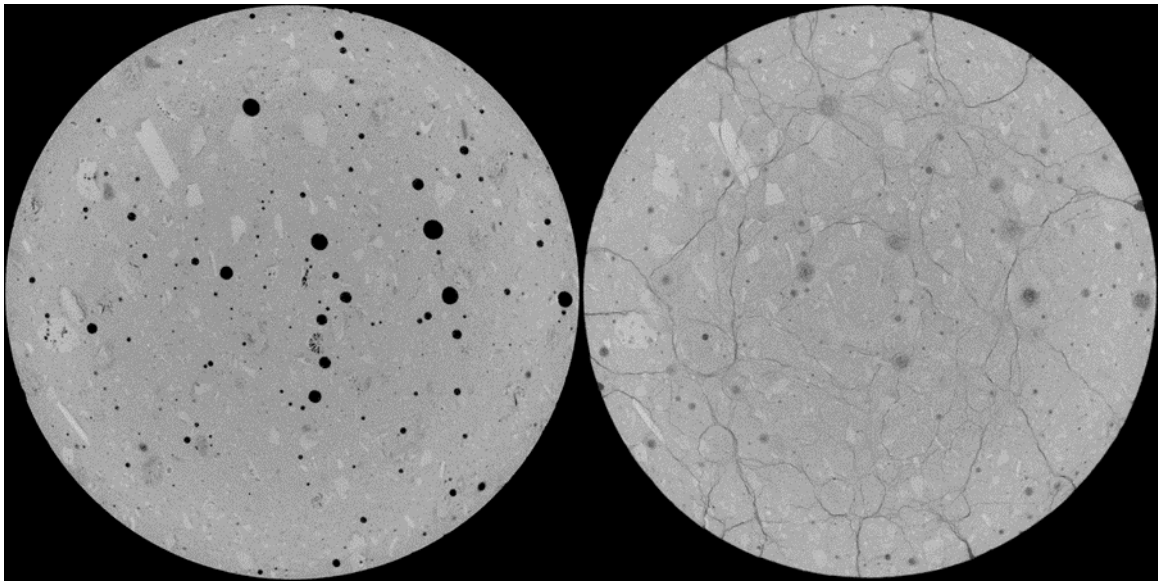

Distribution Statement A. Approved for public release: distribution is unlimited.

The US Army Engineer Research and Development Center (ERDC) solves the nation's toughest engineering and environmental challenges. ERDC develops innovative solutions in civil and military engineering, geospatial sciences, water resources, and environmental sciences for the Army, the Department of Defense, civilian agencies, and our nation's public good. Find out more at www.erdc.usace.army.mil.

To search for other technical reports published by ERDC, visit the ERDC online library at https://erdclibrary.on.worldcat.org/discovery.

ERDC/GSL TR-23-18
December 2023

Residual Strength of a High-Strength Concrete Subjected to Triaxial Prestress

George H. Vankirk, Andreas O. Frank, Michael J. Roth, Brett A. Williams, and William F. Heard

US Army Engineer Research and Development Center (ERDC)
Geotechnical and Structures Laboratory (GSL)
3909 Halls Ferry Road
Vicksburg, MS 39180-6199

Final Technical Report

Distribution Statement A. Approved for public release: distribution is unlimited.

Prepared for US Army Corps of Engineers (USACE)
Washington, DC 20314-1000

Under Program Element No. 0602144A, Project No. BL9, "Protection from Advanced Weapons Effects Technology," Task No. SBL902.

Abstract

This study investigates simplified mechanical loading paths that represent more complex loading paths observed during penetration using a triaxial chamber and a high-strength concrete. The objective was to determine the effects that stress-strain (load) paths have on the material's unconfined compressive (UC) residual strength. The loading paths included hydrostatic compression (HC), uniaxial strain in compression (UX), and uniaxial strain load biaxial strain unload (UXBX). The experiments indicated that the load paths associated with nonvisible microstructural damage were HC and UX—which produced minimal impact on the residual UC strength (less than 30%)—while the load path associated with visible macro-structural damage was UXBX, which significantly reduced the UC strength (greater than 90%). The simplified loading paths were also investigated using a material model driver code that was fitted to a widely used Department of Defense material model. Virtual experiment data revealed that the investigated material model overestimated material damage and produced poor results when compared to experimental data.

DISCLAIMER: The contents of this report are not to be used for advertising, publication, or promotional purposes. Citation of trade names does not constitute an official endorsement or approval of the use of such commercial products. All product names and trademarks cited are the property of their respective owners. The findings of this report are not to be construed as an official Department of the Army position unless so designated by other authorized documents.

DESTROY THIS REPORT WHEN NO LONGER NEEDED. DO NOT RETURN IT TO THE ORIGINATOR.

Contents

Figures and Tables

Figures

Tables

Preface

This study was conducted for the US Army Corps of Engineers under Program Element No. 0602144A, Project No. BL9, "Protection from Advanced Weapons Effects Technology," Task No. SBL902.

The work was performed by the Concrete and Materials Branch (GMC) and the Impact and Explosives Effects Branch (GMI) of the Engineering Systems and Materials Division (GM) and the Survivability Engineering Branch (GSV) of the Geosciences and Structures Division (GSD). At the time of publication, Dr. Jay Shannon was chief, GMC; Jeffrey G. Averett was chief, GMI; Mr. Justin S. Strickler was chief, GM; Mr. Omar G. Flores was chief, GSV; Mr. James L. Davis was chief, GS; and Ms. Pamela G. Kinnebrew was the lead technical director for Military Engineering. The deputy director of ERDC-GSL was Mr. Charles W. Ertle, and the director was Mr. Bartley P. Durst.

COL Christian Patterson was the commander of ERDC, and Dr. David W. Pittman was the director.

1 Introduction

1.1 Background

Penetration into concrete has historically been a widely-studied area of research (White 1946; Forrestal 1985; Warren et al. 2004; Forrestal et al. 1994; Hanchak et al. 1992; Gran and Frew 1996), with some of the original research emerging during World War II (White 1946). While the focus of this study is not to directly study the effects of penetration into concrete, it does aim to investigate simplified mechanically induced stress paths that have been classically used to investigate concrete materials' response to penetration modeling. Specifically, this study seeks to investigate the residual strength of concrete subjected to simplified stress paths, which are representative of more complex stress paths observed in penetration events.

The study of the residual strength of concrete subjected to penetration centric stress paths is of interest to both the civil and military communities. Concrete is the most widely used building material in the world by volume with over 25 billion tons produced annually (Cement Suitability Initiative 2009). Concrete's high rate of consumption can be attributed to three main reasons: (1) concrete structures are extremely durable, (2) fresh concrete is easily formed into a variety of shapes, providing great flexibility to the design of structural elements, and (3) concrete is often the most cost-efficient and readily available building material (Mehta and Monteiro 2006). These reasons naturally lend concrete to be the building material of choice for civil structural applications. For military applications, protection against highly impulsive events such as blast and penetration are required, and so concrete is typically the preferred material of choice.

During highly impulsive events, such as blast and penetration, materials subjected to the resultant dynamic loads display complex stress states. Concrete, unlike most metals, has both strain rate and pressure dependencies on its strength, therefore it can be challenging to quantify material damage in concrete as a result of highly impulsive events. High-velocity penetration into concrete can generate a large amount of impact pressure at very high strain rates, creating the opportunity for multiple complex damage mechanisms to take place. For insight into how these damage mechanisms develop, some of the phenomena associated with projectile penetration into concrete are discussed.

Concrete is typically associated with a high unconfined compressive strength and a relatively weak tensile strength in comparison. The initial high shock loading of the projectile on a concrete surface imparts both tensile and compressive waves that travel through the concrete material, which produces damaging effects. One damage mechanism, observed as a result of penetration into concrete, is spalling at the free surfaces due to reflection of incident-compressive impulses generated by the shock loading of the projectile (Nordendale et al. 2015). In the first few microseconds of projectile impact, material damage in the form of cratering takes place. The material directly ahead of the path of the projectile undergoes local material compaction. The high rate of the penetration event leads to an imposed radial inertial confinement, which would otherwise allow for the material to undergo outward expansion. Therefore, the material in front of the projectile essentially undergoes radially confined compression. These phenomena, namely material compaction and radial inertial confinement, combined with the observation that concrete's strength evolves with confining pressure, has classically prompted the study of triaxial compression test results when attempting to study how concrete material behaves under complex loading such as penetration. More specifically, the load paths of hydrostatic compression, uniaxial strain compression, and simple triaxial compression with constant radial pressures (Nordendale et al. 2015) bear further study.

As previously described, the penetration process and resulting damage can be challenging to understand, and an even greater challenge would be to attempt to replicate the complex stress paths present during actual penetration events. Hence, instead of replicating many complex stress paths, simplified material characterization can be performed using stress paths relevant to the penetration process. Hydrocodes, used to numerically investigate penetration into concrete material, typically use material constitutive models that are fit to simplified mechanical characterization data (Nordendale et al. 2015; Frank 2012; Holmquist et al. 1993; Frank and Adley 2011).

Figure 1 and Figure 2 show hydrocode-calculated stress paths using the High-Rate Brittle (HRB) model (Frank 2012) and the EPIC hydrocode (Johnson et al. 2001) during a concrete penetration event at Mach 1. Shown are the shear stress versus pressure at various depths and radii within the target normalized with respect to the projectile radius, two radii ($2R$) and three radii ($3R$). Qualitatively, the form taken by these observed stress paths

are similar to a uniaxial strain loading followed by biaxial strain unloading (UXBX) condition. Simplified mechanical stress paths in a triaxial chamber can produce a uniaxial strain loading condition and the resultant biaxial strain unloading condition. The similarity of the hydrocode simulation to the classic laboratory UXBX stress path may be explained by the inertial response of the concrete target.

Figure 1. Hydrocode-calculated stress paths during projectile penetration into concrete at Mach 1. Taken at a normalized radius of two radii (2*R*).

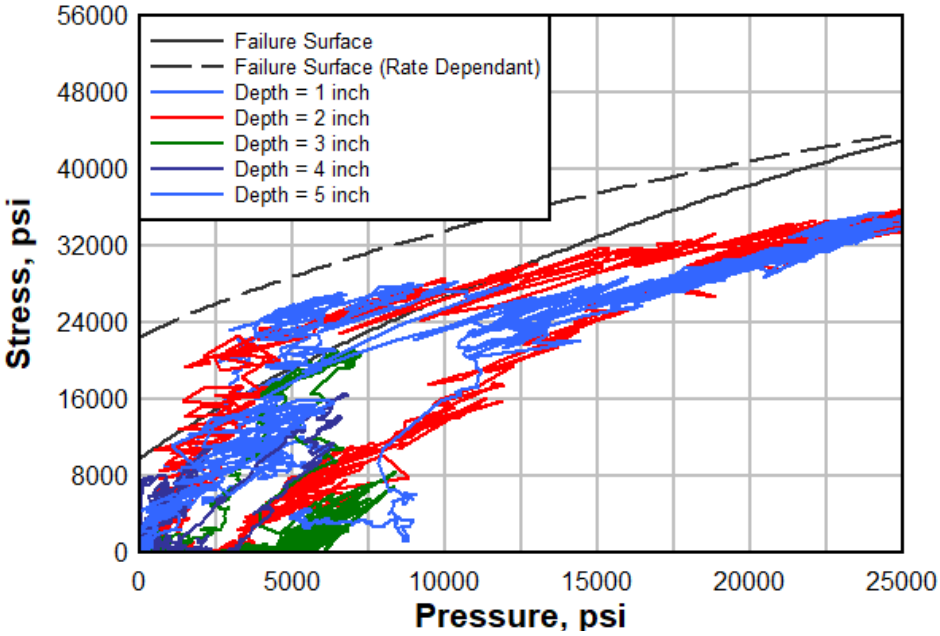

Figure 2. Hydrocode-calculated stress paths during projectile penetration into concrete at Mach 1. Taken at a normalized radius of three radii (3*R*).

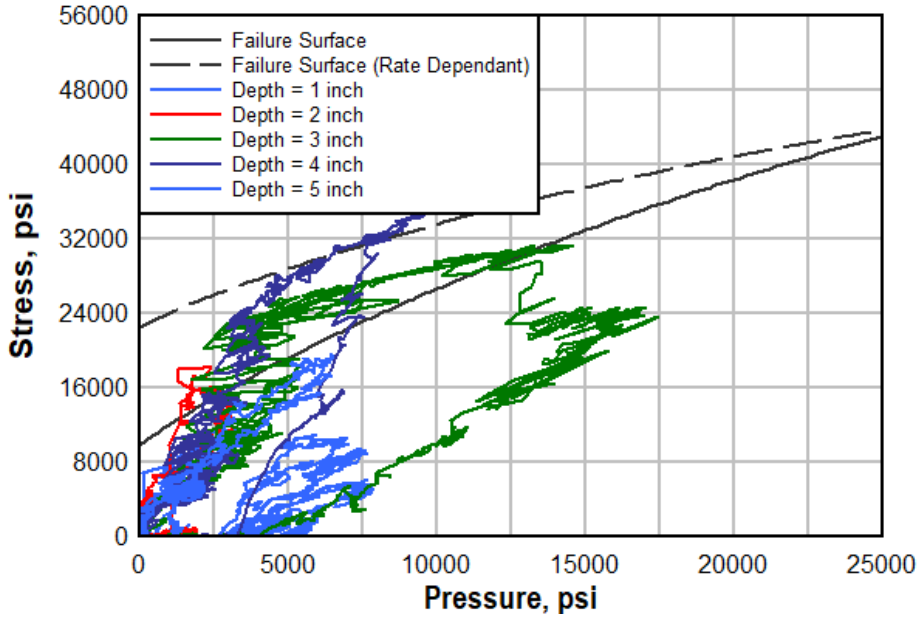

As previously mentioned, concrete strength is both strain rate and pressure dependent. Material characterization data for concrete are typically gathered by physical experiments designed to isolate the material response of interest; thus, strain rate and pressure dependent strength are often investigated independently. The strain rate dependency of concrete is often investigated using a Kolsky bar technique (Kolsky 1949), which is based on one-dimensional stress-wave theory in elastic solids. The strain-dependent strength of concrete—while an important research area with respect to highly impulsive events such as penetration—is not the focus of this study.

Many studies have been published using the GIGA press—located at the 3SR facility in France—to test concrete with confining pressures up to 850 MPa* (Malecot et al. 2009; Forquin and Piotroska 2015; Vu et al. 2008; Gabet et al. 2008; Forquin et al. Zaera 2009). Some alternative methods of triaxial compression use cubes that can be loaded independently in the three principal directions (Lu et al. 2003). Other methods include more complex loading paths utilizing a rigid ring to radially confine concrete as axial load is applied (Forquin et al. 2007). This type of loading is referred to as quasi-oedometric compression and can reach pressures up to 500 MPa. (Bazant et al. 1986) noted that the standard triaxial test may not simulate the condition of structures designed to resist explosions or impact. In these structures, concrete is confined by heavy reinforcement in three directions, which causes the lateral normal stresses to increase along with the axial stress.

The most common method for performing successful compression of concrete uses a sealed specimen within a steel chamber that provides active confinement through the application of fluid pressure. In this method, a cylindrical specimen is sealed with a membrane (butyl, latex, and neoprene) to prevent ingress of confining fluid. Then, a hydraulic fluid fills the chamber and is pressurized by a servo-controlled system to apply a desired hydrostatic pressure. When confining pressure is maintained, the loading piston is activated to apply a deviatoric stress in the axial direction. By applying fluid pressure, friction effects are reduced (Williams et al. 2006). Pressurized fluid chambers have the advantage of reaching high-pressure confinement. Servo-controlled loading of pressurized triaxial cells also offer

* For a full list of the spelled-out forms of the units of measure used in this document, please refer to *US Government Publishing Office Style Manual*, 31st ed. (Washington, DC: US Government Publishing Office, 2016), 248–52, https://www.govinfo.gov/content/pkg/GPO-STYLEMANUAL-2016/pdf/GPO-STYLEMANUAL-2016.pdf.

the capability of exercising the material through a variety of loading and unloading paths, which may be more representative of penetration events.

Constitutive model development and calibration efforts using triaxial compression testing in this fashion have been conducted at the US Army Engineer Research and Development Center (ERDC) for decades (Akers et al. 1986; Williams et al. 2006; Williams et al. 2009). There is a significant amount of triaxial stress data for various concretes in the literature; however, very seldom is a sample tested, recovered, and then a determination of its residual strength quantified.

1.2 Objectives

The objectives of this study are to (1) determine the triaxial response of a high-strength concrete in order to fit and evaluate a constitutive model, (2) subject specimens of the same concrete material to simplified mechanical loading paths that represent the more complex loading paths seen during penetration events, and (3) recover the samples subjected to these simplified load paths and quantify their residual strength. X-ray micro-computed tomography imaging (micro-CT) of samples subjected to the same load paths was also performed in order to view the microstructure of the material after loading. The simplified loading and unloading paths of interest include pure hydrostatic compression, uniaxial strain in compression, and uniaxial strain in compression loading followed with biaxial strain in compression unloading. Peak loading of the specimens was provided at both low and high confining pressures corresponding to quasi-brittle and ductile material responses, respectively. A constitutive model (Adley et al. 2010) widely used by the DoD in various hydrocodes (Johnson et al. 2001; Adley et al. 2010; McGlaun et al. 1990) has been fitted to the laboratory data and evaluated with respect to the residual capacities determined herein.

1.3 Approach

The purpose of this study is to quantify the pressure-dependent strength of a high-strength concrete and the resulting damage mechanisms with respect to its residual strength. Simplified mechanical stress paths are used to investigate how both applied pressure and stress path affect a concrete's residual strength. To accomplish concrete loading through simplified mechanical stress paths, a servo-controlled fluid triaxial chamber—which

can apply fluid confining pressure and axial loading simultaneously—will be used.

The specific stress paths of interest for this study include hydrostatic compression (HC), uniaxial strain compression (UX), and simple triaxial compression with constant radial pressure (TXC). These stress paths have been historically used to develop concrete constitutive models (Nordendale et al. 2015; Frank 2012; Holmquist et al. 1993; Frank and Adley 2011). The work to understand concrete's pressure-dependent strength utilizing triaxial compression was pioneered by Balmer (1949). Triaxial experiments performed on concrete specimens are similar to those documented for soils (Bishop and Henkel 1957) but require much higher confining pressure.

Since the initial work by Balmer, extensive work has been conducted to determine the triaxial properties of normal strength concrete (Imran and Pantazopoulou 1996; Malecot et al. 2009; Forquin and Piotroska 2015; Vu et al. 2008; Gabet et al. 2007; Sfer et al. 2002; Forquin et al. 2009; Lu et al. 2003; Forquin et al. 2007; Bazant et al. 1986; Chuan-Zhi et al. 1987). The focuses of these efforts have been to discover the relationship between confining pressure and peak stress. As confining pressure increases, so does the compressive strength of concrete. Concrete also exhibits a brittle response at low confining pressure and a more ductile response at higher confining pressures. Ultimately, the failure of concrete under triaxial compression is marked by uncontrolled volumetric expansion (Imran and Pantazopoulou 1996).

It has also been discovered that the unconfined compressive strength of concrete does not have much effect on the high-pressure triaxial response, while the saturation level does have an impact on the high-pressure triaxial response (Imran and Pantazopoulou 1996; Malecot et al. 2009; Forquin and Piotroska 2015; Vu et al. 2008). Saturated samples exhibit increased ductile behavior under high confinement levels, and the apparent concrete strength increases under high confinement as concrete dries.

Experimental work has also been performed on the influence of the loading path on the compaction of concrete under confinement (Gabet et al. 2008). Compaction in concrete can be explained by a coupling of initial elastic behavior and two irreversible phenomena that occur simultaneously (i.e., pore collapse and structural decohesion of the cement matrix). Loading paths that manifest in high shear stress environments produce increased

compaction, and under high shear stress, granular stacking occurs within the cement matrix (Gabet et al. 2008).

Experimental studies on the triaxial properties of concrete typically focus on the initial loading of the material and determination of peak stress. Under the work of Sfer (Sfer et al. 2002), large specimens (150 mm × 300 mm) of conventional strength concrete (30 MPa) were subjected to confining pressures up to 60 MPa, which produced axial strains of over 10%. The residual unconfined compressive strength of the damaged material was determined. A reduction of 60% in unconfined compressive and 50% in the elastic modulus was observed.

2 Materials and Methods

2.1 Material and Specimen Preparation

The high-strength concrete material investigated in this study is referred to in the literature as BBR9 (Williams et al. 2019; Vankirk et al. 2019). BBR9 has a maximum aggregate size of 4.75 mm and is a self-consolidating concrete. BBR9 contains the following constituent materials: manufactured limestone sand, type I and II portland cement, grade 100 ground granulated blast-furnace slag (slag), undensified microsilica (silica fume), polycarboxylate-ether-based high-range water-reducing admixture (HRWA), and tap water. Mixture proportions for BBR9 are presented in Table 1 and are based on a unit volume.

Table 1. BBR9 mixture composition.

Constituent	Mix Proportions, by volume
Cement (Type I–II)	0.1636
Manufactured limestone sand	0.4513
Slag	0.1048
Microsilica (silica fume)	0.0612
Water (tap)	0.2035
High-range water-reducing admixture	0.0156

Development of BBR9 used the central composite design of experiments and focused on dense particle packing, minimization of flaws, and maximum calcium silicate hydrate as described in prior publications (Ragalwar et al. 2016; Ragalwar et al. 2017). The material for this study was mixed using a high-shear Sicoma M565/375 planetary mixer with a maximum capacity of 0.8 m^3. Rheological property measurements included determining a spread value in accordance with ASTM C230 (2021).

After the concrete was mixed, it was placed in 75 mm × 150 mm cylinders and large blocks with approximate dimensions of 60 cm × 45 cm × 30 cm for the purpose of coring at a later date. Specimens were wet cured with burlap for 30 hours, then placed under insulation blankets and steam cured for three days while maintaining a temperature of 90°C and 100% humidity. Due to the steam curing process, the majority of unconfined compressive strength gain occurred in the first seven days. Specimens were cored and finished to achieve parallelism and flatness in accordance with ASTM C42 (2020). Average

finished specimen dimensions were 50.8 mm × 114.3 mm. Unconfined compression strength was determined according to ASTM C39 (2018).

2.2 Experimental Approach

The following experiments were conducted: (1) initial unconfined compression (UC) experiments to evaluate the undamaged strength of the material, (2) triaxial compression experiments to develop a constitutive model fit, (3) strain-path tests including HC, UX, and UXBX at low and high confining pressures to prestress the material, and (4) unconfined compression testing on prestressed specimens to evaluate their residual strength. All mechanical property tests were performed using servo-hydraulic loading and were conducted quasi-statically at strain rates of 10^{-5} and 10^{-4} s^{-1}. Two different pressure levels were used in the strain-path tests to investigate material response during quasi-brittle and ductile behaviors. The pressure levels for the strain-path tests were chosen based on the TXC material response. Table 2 lists a test matrix for the experiments conducted.

Table 2. Test matrix for residual strength study.

Type of Test	No. of Tests	Nominal Peak Radial Stress (MPa)
Baseline UC	30	0
TXC	2	0
	2	10
	2	20
	2	50
	2	100
	2	200
	2	300
HC	5	133
	5	400
UX	5	85
	5	330
UXBX	5	133
	5	400
Residual UC	30	0

2.3 Triaxial Test Equipment and Instrumentation

Triaxial compression experiments were conducted at ERDC using a 600 MPa-capacity pressure vessel that is paired with an 8.9 MN universal

testing machine used to provide axial loads. A 50/50 mixture of hydraulic oil and kerosene was used as the confining fluid. Hardened steel caps were placed on the ends of the sample, and then two 0.6 mm-thick latex membranes and an Aquaseal® membrane were positioned around the specimen. An additional latex membrane was placed outside of the assembly and sealed with a liquid nitrile rubber. The purpose of this setup was to prevent ingress of confining fluid during the testing protocol. An MTS FlexTest controller and data acquisition system were used for the servo-controlled testing conditions and allowed for testing conditions to be made based on displacement, load, or pressure to achieve the desired stress or strain path.

A vertical deflection measurement system was used for all confined tests to measure axial deformation of the samples. The system consisted of two linear variable differential transformers (LVDTs). The LVDTs were mounted vertically on the instrumentation stands and positioned 180° apart. The orientation and mounting position on the top and bottom base caps allowed for displacement measurements (i.e., as the base caps move in opposition of each other, the distance between them changes). This change in distance corresponds to a change in electrical resistance as measured by the LVDT, and this change in resistance can be directly correlated to a measured strain within the material. On tests that required hydraulic confinement, a linear potentiometer was mounted externally on the pressure vessel to measure the piston through which axial loads were applied. The externally mounted potentiometer provided a backup to the vertical LVDTs in case they exceeded their calibrated range.

Radial deflection measurements were made using two types of lateral deformeter systems. For all strain path tests, two small steel footings were mounted 180° apart, directly to the specimen at the mid-height. These footings were machined to align with the curvature of the test specimen. On the end opposite from the machined face, threaded posts extended and protruded through the latex membrane, allowing for mounting points for instrumentation. A lateral deformeter ring was mounted to the threaded posts. The output of each deformeter was calibrated to the radial displacement of the steel footings. An LVDT was mounted on a hinged ring that attached to the two steel posts mounted on the specimen. The LVDT measured the expansion and contraction of the ring. When the specimen expanded (or contracted), the hinged ring opened (or closed), which caused a change in the electrical current. This change in current was related to the

radial strain in the specimen. This type of lateral deformeter was used for all the HC, UX, and UXBX tests.

For the TXC tests, a second type of lateral deformeter was used. This lateral deformeter consisted of two strain-gaged steel spring arms mounted on a double-hinged ring. When the specimen expanded or contracted, the rigid deformeter ring flexed about its hinge, causing a change in the electrical output of the system. This setup was used when larger radial strains were expected and is a less accurate measurement system than the LVDT.

2.4 Definitions of Stresses and Strains

The specimen geometry was assumed to be a right circular cylinder under infinitesimal deformations. Measurements of radial strain (ε_r) and axial strain (ε_a) were continuously recorded. Volumetric strain (ε_v) was calculated as the sum of the axial strain and twice the radial strain. Stress values are reported in terms of true stress, since they are based on the changing cross-sectional area of the specimen. The principal stress difference (PSD) is defined as the difference between radial stress (σ_r) and axial stress (σ_a). The mean normal stress (MNS) or pressure is calculated as the average of the applied principal stresses.

2.5 Triaxial Compression with Constant Radial Pressure Experiments

To quantify the material's pressure-dependent strength characteristics and provide data for constitutive model fitting, triaxial compression experiments with constant radial pressure were performed on BBR9 specimens (Adley et al. 2010). Duplicate experiments were conducted under radial confining pressures of 0, 10, 20, 50, 100, 200, and 300 MPa. The materials' responses at each level of confining pressure are plotted in Figure 3 in terms of PSD versus ε_a and in Figure 4 in terms of PSD versus MNS, or stress path space.

Figure 3. Triaxial response of concrete specimens at confining pressures of 0, 10, 20, 50, 100, 200, and 300 MPa in terms of principal stress difference (PSD) versus ε_a.

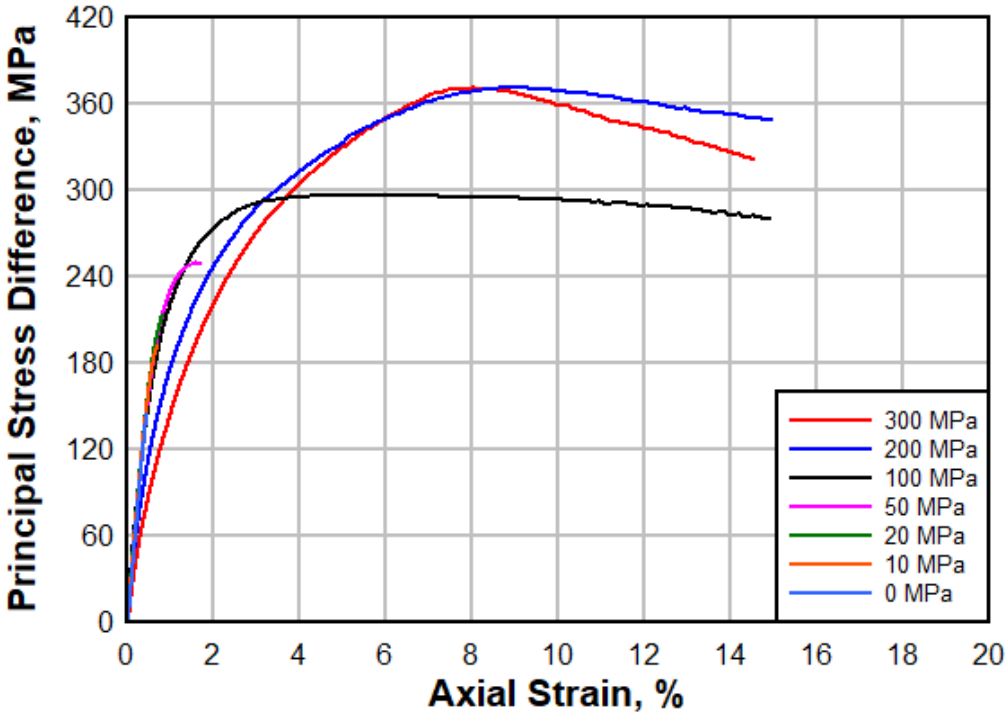

Figure 4. Triaxial stress paths and peak strength values plotted in terms of PSD versus mean normal stress (MNS).

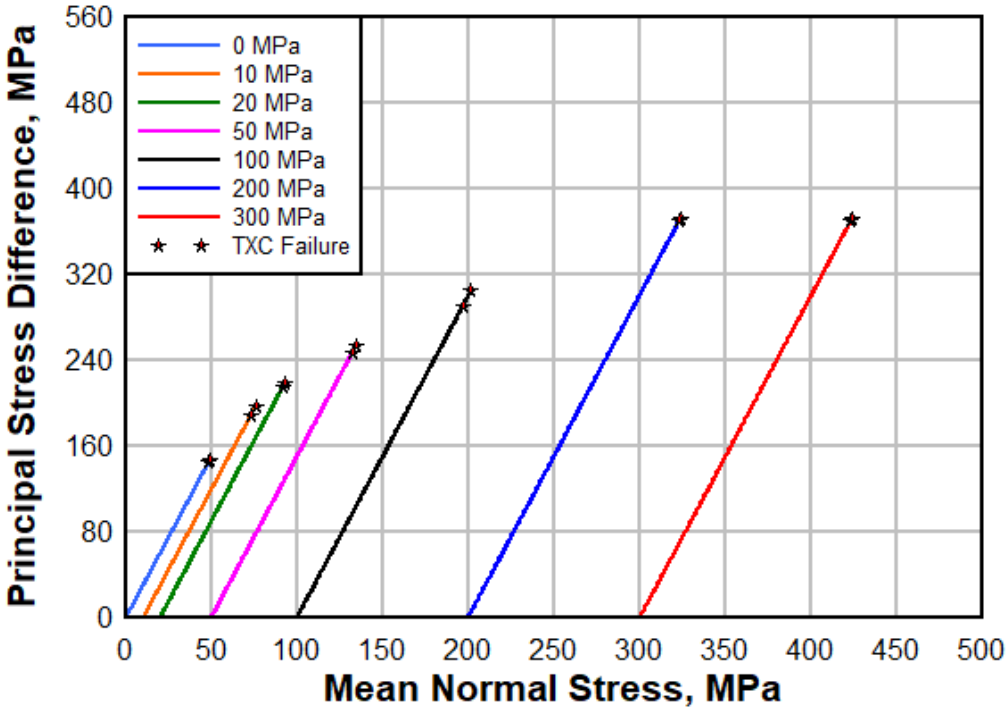

The peak material strength increases with increased confining pressure. The peak strength values can be used to construct a limit surface for the shear strength in PSD versus MNS space. Since the strength data are limited both near the origin of the PSD versus MNS plot and at high levels of confinement (greater than 500 MPa), it can be difficult to fit a material model in those regions (Frank and Adley 2011). Concrete and rock generally exhibit quasi-brittle behavior at low pressures with a more ductile-like response at higher pressures. As in Figure 3, large postpeak axial strain levels can be seen for confining pressures above 100 MPa, which corresponds to a postpeak MNS of greater than 200MPa. This infers some ductility in the deformation of the sample. However, for confining pressures below 50 MPa, which corresponds to a postpeak MNS of less than 133 MPa, it was not possible to capture the postpeak response of the material due to an abrupt loss of strength. This infers a quasi-brittle behavior in the deformation of the sample. Thereby, the peak MNS loading considered for prestressing the samples were 133 and 400 MPa, to provide low-pressure quasi-brittle and high-pressure ductile respectively.

2.6 Hydrostatic Compression Prestress Experiments

Prestress experiments were conducted for HC loading to peak MNS levels of 133 and 400 MPa followed by HC unloading of the samples. Hydrostatic compression subjects the concrete specimens to global volumetric compaction without a mechanically induced global shear stress, since both axial and radial stresses remain equal. However, local shear within the cement matrix may still exist due to local stress concentrations generated by a heterogeneous material with voids. The material response data for each stress-strain path are plotted in Figure 5 in terms of MNS versus ε_v and Figure 6 in terms of PSD versus MNS. The stress-strain paths for the lower pressures tested are presented in blue and the stress-strain path for the higher pressures tested are presented in red. All of the data have been presented in order to display the variability between tests under idealized conditions.

For experiments conducted up to 133 MPa MNS, peak volumetric strain values were approximately 0.6% with no observable permanent volume strain or compaction (nearly linear elastic behavior). For high-confinement tests (400 MPa), the application of pressure was intentionally held constant at 400 MPa for a period of 100 seconds before unloading. During the hold in pressure, the volume strains continued to slightly increase less than 0.5%, indicating that the concrete is susceptible to creep at high stress levels.

Inelastic volume strains were observed at a pressure level of approximately 180 MPa and at a volumetric strain of approximately 0.8%. The permanent volume compaction observed was greater than 1%. The initial elastic bulk modulus was approximately 21 GPa. The resulting stress paths for the HC loading experiments follow along the mean normal stress axis as expected.

Figure 5. Material response data for hydrostatic compression (HC) tests at 133 and 400 MPa in terms of MNS versus ε_v.

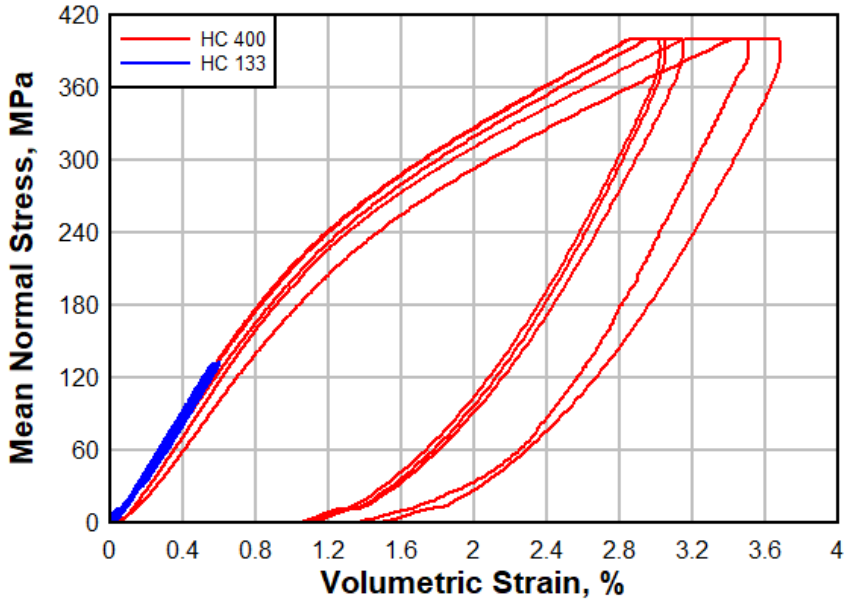

Figure 6. Material response data for HC tests at 133 and 400 MPa in terms of PSD versus MNS with peak triaxial compression (TXC) values.

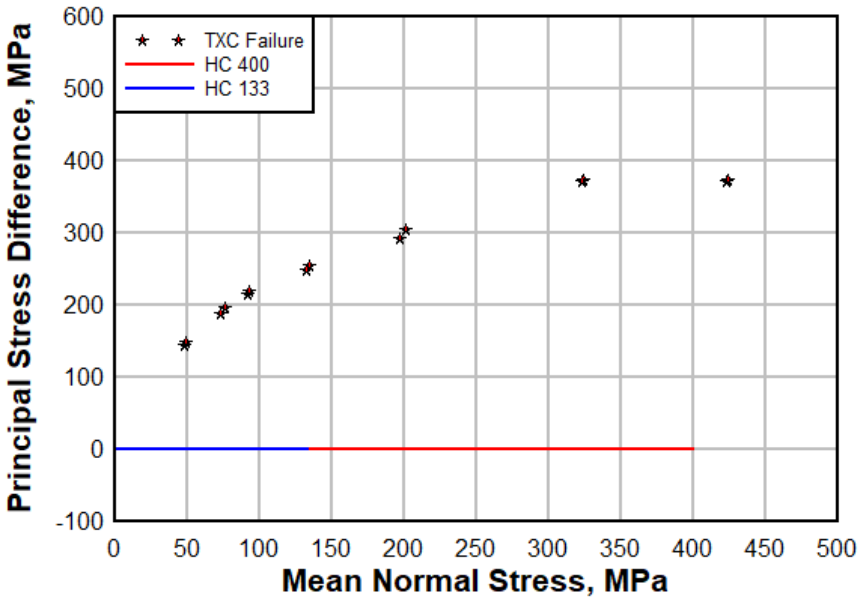

2.7 Uniaxial Strain in Compression Prestress Experiments

Uniaxial strain in compression subjects the concrete specimens to both global volumetric compaction with a mechanically induced global shear stress, since the axial stress is necessarily greater than the radial stress. The material response data are plotted in Figure 7 in terms of MNS versus ε_v and Figure 8 in terms of PSD versus MNS. The stress-strain paths for the lower pressure tested are presented in purple, and the stress-strain path for the higher pressure tested are presented in black. All of the data have been presented in order to display the variability between tests under idealized conditions. The specimens subjected to the UX loading display greater volumetric strains than the HC loading due to shear-induced dilation that is common for concrete. Volumetric strains of approximately 0.7% and 4% were observed for samples with peak MNS loading of 133 and 400 MPa, respectively.

Figure 7. Material response data for uniaxial strain compression (UX) tests at 133 and 400 MPa in terms of MNS versus ε_v.

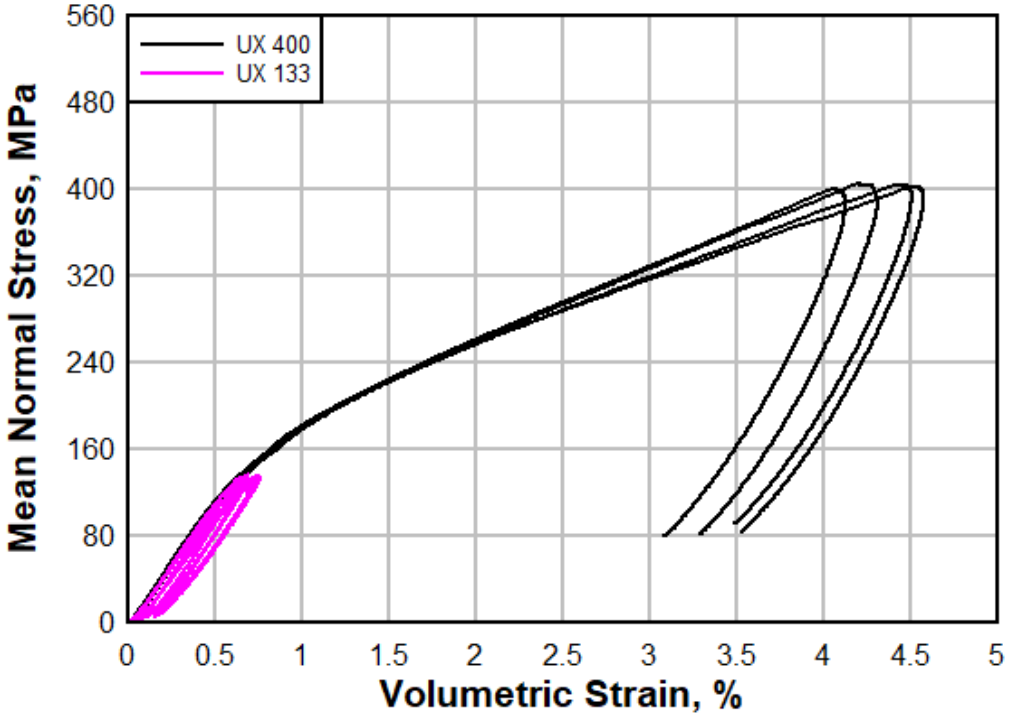

Figure 8. Material response data for UX tests at 133 and 400 MPa in terms of PSD versus MNS with peak TXC values.

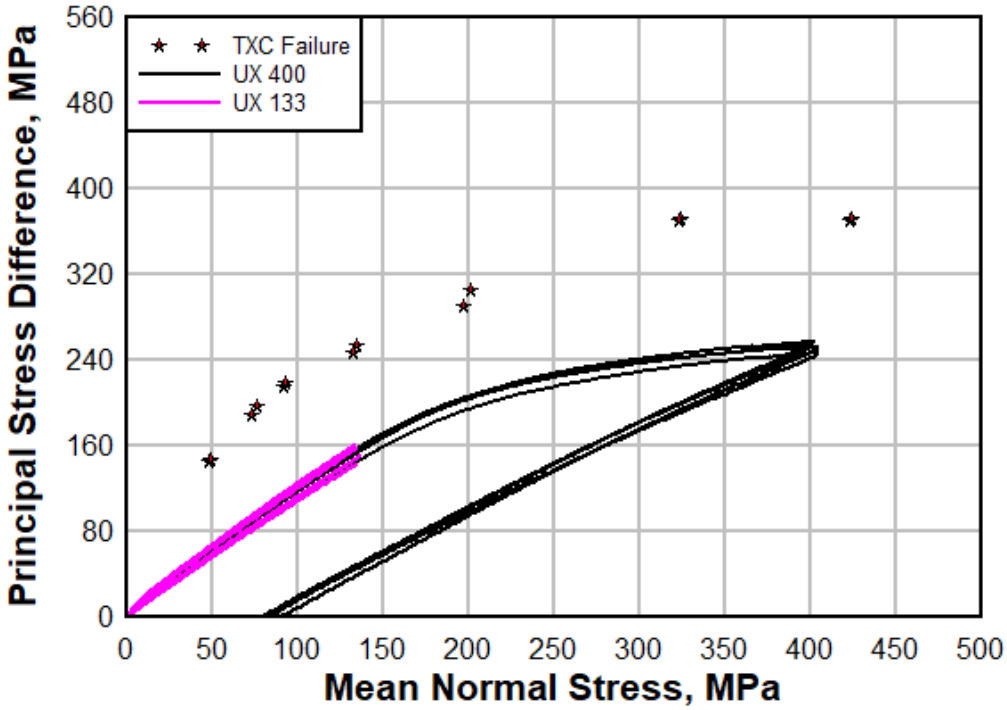

In stress path space, the slope for the initial elastic portion of loading represents $2G/K$, where G is the shear modulus, and K is the bulk modulus. The initial elastic shear modulus was calculated as 11.5 GPa, resulting in an initial Young's modulus I of 29 GPa and Poisson's ratio of 0.26. The UX stress paths trend below the peak TXC values or the limit surface. For the low-pressure experiments (peak MNS of 133 MPa), the material exhibits nearly elastic behavior, which can be seen from both the pressure versus volume strain and PSD versus MNS plots.

2.8 Uniaxial Strain Load Biaxial Strain Unload Prestress Experiments

Prestress experiments were conducted for UX loading to peak MNS levels of 205 and 500 MPa, followed by biaxial strain (BX) unloading of the samples. The UX loading of the samples is identical to that described in Section 3.3; however, during unloading, the sample is subjected to a state of forced volumetric expansion induced by a biaxial strain that occurs from holding the axial strain constant while the confining pressure is decreased. As previously mentioned, this stress path may be representative of the initial confined state concrete experiences during penetration, and the late-time relaxation during cratering. The material response data are plotted in Figure 9 in terms of MNS versus ε_v and Figure 10 in terms of PSD versus MNS. The

stress-strain paths for the lower pressure tested are presented in green, and the stress-strain path for the higher pressure tested are presented in orange. All the data have been presented in order to display the variability between tests under idealized conditions.

During the loading phase, the material undergoes UX compression similar to what is described in Section 3.3, although at different peak MNS levels. This results in higher peak volumetric strain values of approximately 1.5% and 6.5% for peak MNS levels of 205 and 500 MPa, respectively. In between the UX and BX loading, the material undergoes a stress relaxation during the system change that requires 200 seconds to complete for the higher pressure tested and 40 seconds to complete for the lower pressure tested. During the BX unloading phase, volumetric strains decrease gradually while the material is still subjected to high confining pressures and decrease sharply when the shear limit has been met. This can be clearly seen from the stress path plot where the shear limit can be inferred from the peak TXC values. The MNS-ε_v, data also indicate a large amount of volume recovery that occurs during the BX unloading, to an extent that crosses the datum into negative or tensile volumetric strains. Such tensile volume strains indicate that the samples may be heavily damaged macroscopically.

Figure 9. Material response data for uniaxial strain load biaxial strain unload (UXBX) tests at 205 and 500 MPa in terms of MNS versus εv.

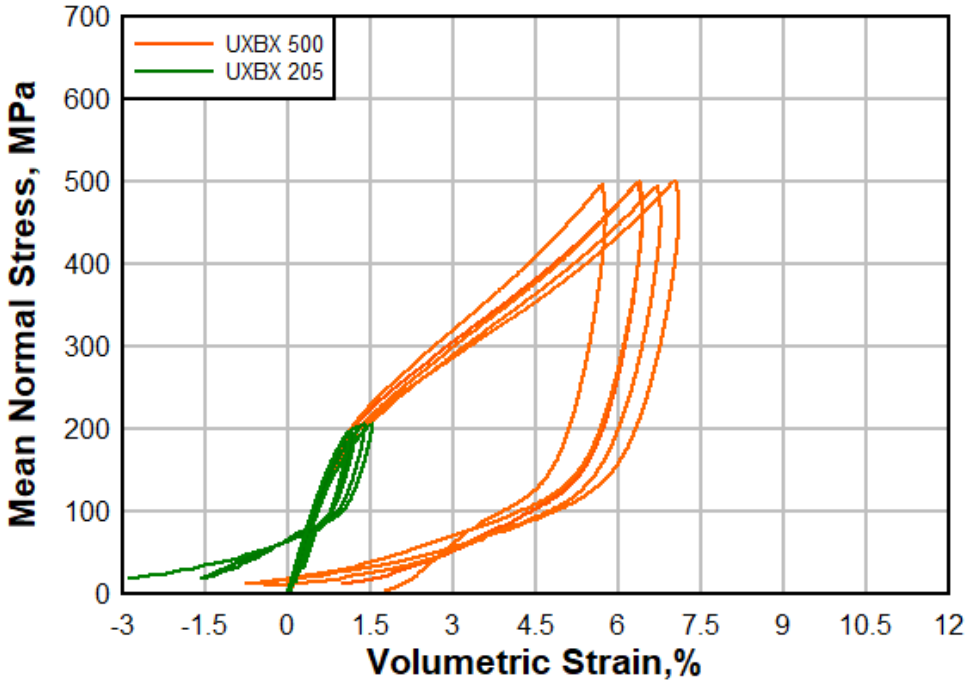

Figure 10. Material response data for UXBX tests at 205 and 500 MPa in terms of PSD versus MNS with peak TXC values.

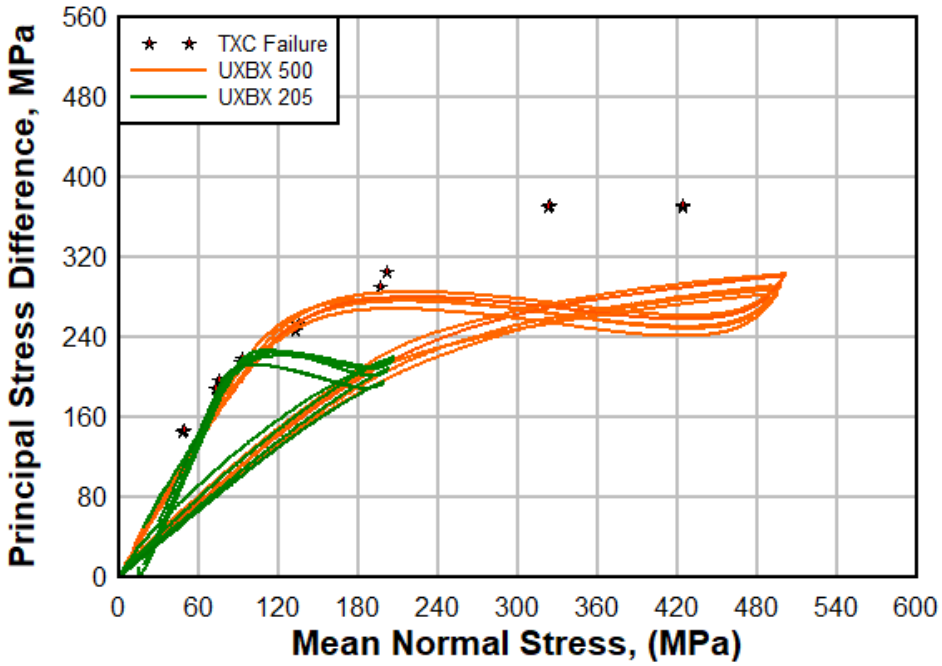

2.9 X-Ray Micro-Computed Tomography (Micro-CT) Imaging Analysis

To investigate the materials' microstructural change as a result of triaxial loading, specimens of the same concrete batch were subjected to micro-CT imaging both before and after loading. Micro-CT imaging allows for nondestructive high-resolution 3D imaging and measurement of material morphology. In micro-CT scans of heterogeneous solids such as concrete, the various constituent phases (e.g., cement matrix, aggregate, and voids) can be segmented based on their relative X-ray attenuation rates (Loeffler et al. 2018). One specimen for each stress-strain path (HC, UX, and UXBX) was scanned pre and postloading at a MNS level of 400 MPa in order to highlight the damage mechanisms present when tested at such high pressures.

The specimens were examined using a Nikon XT 255 ST high-resolution micro-CT scanner. The nominal resolution for each scan used a cubic voxel with a side length of 29.5 μm. An acceleration voltage of 217 kV was used to pass X-rays through a 1 mm thick tin filter before penetrating the sample. During each scan, the specimen was rotated a total of 360° with a step size of 0.112° resulting in 3,141 projection images. Central portions of the corresponding scans (pre and postmechanical loading) were synced to facilitate image analysis, as these portions of the cylindrical specimen

should have been subjected to the highest levels of damage. Transverse views of image slices taken from the central portion of the HC, UX, and UXBX pristine and damaged scans are provided in Figure 11, Figure 12, and Figure 13.

Figure 11. Micro-CT images of concrete specimen subjected to HC loading; pristine image shown on left and postloading image shown on right.

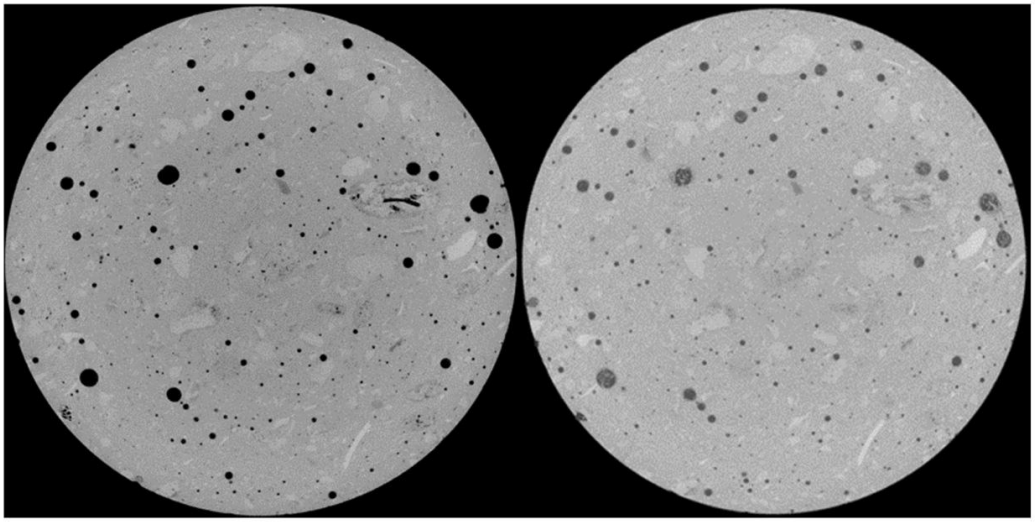

Figure 12. Micro-CT images of concrete specimen subjected to UX loading; pristine image shown on left and postloading image shown on right.

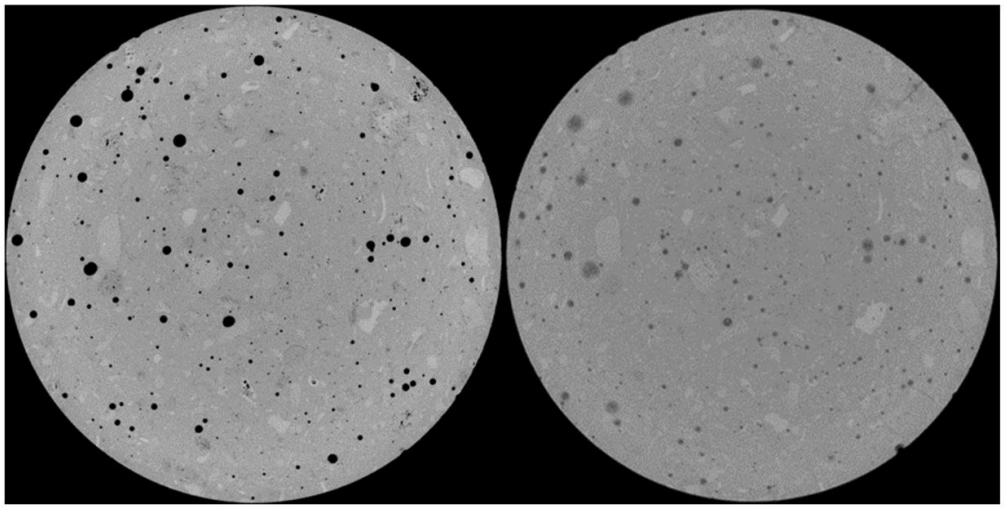

Figure 13. Micro-CT images of concrete specimen subjected to UX loading; pristine image shown on left and postloading image shown on right.

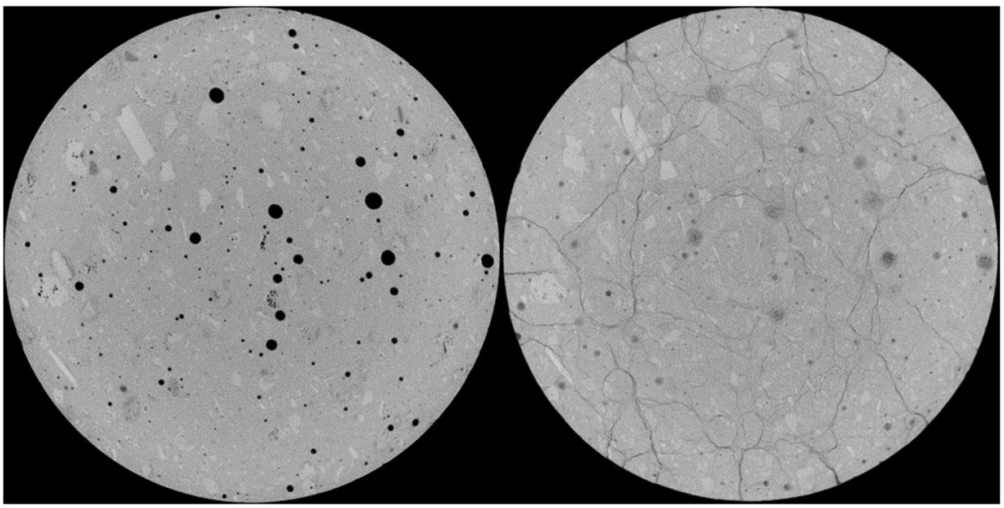

For all loading conditions, some pore collapse and void closure is evident; however, the extent of void closure is not at its maximum since the samples have fully relaxed during unloading and only show permanent volume compaction or strains. For the samples that underwent HC and UX prestress loading conditions, the level of material damage is unclear, since visible cracking is not evident. However, it is likely that stress concentrations occurring from local shear around pores induces micro cracks that are not visible at this scanning resolution. For the sample that underwent UXBX prestress loading conditions, both void closure as well as clear evidence of a widespread distributed macro crack are observed. This widespread and distributed crack network is most likely the result of the forced state of volumetric (tensile) expansion due to the BX unloading process.

2.10 Unconfined Residual Strength of Prestressed Samples

To provide a baseline for comparison, BBR9's pristine unconfined compressive strength was determined through a series of 30 tests. These tests were performed on material cored from large 60 cm × 45 cm × 30 cm blocks cast during the initial placement. Prior to destructive testing, diameter, height, and weight were recorded for each specimen. All unconfined compression testing including initial baseline and residual strength were conducted in accordance with ASTM C39 (2018). A closed loop universal testing machine was used to conduct uniaxial compression tests at a stress rate of 0.25 MPa/s. The mean unconfined compressive

strength of the 30 pristine samples was determined to be 141 MPa, with a standard deviation of 11.8 MPa.

After mechanical loading for all HC, UX, and UXBX experiments, each sample was recovered from the hydraulic load cell. The instrumentation and latex membranes were carefully removed as to not disturb the state of the tested concrete. It was possible to conduct UC testing on all but two of the samples. The two samples that could not be tested were from the UXBX prestress loading conditions and were essentially split with large macro-cracks such that the UC strength could be assumed to be zero. The unconfined residual strength data for all of the prestress loading conditions considered are plotted in Figure 14 along with the pristine data for comparison. The average residual strength values are listed in Table 3 with respect to the pristine strength. The HC and UX prestressed samples, which did not observe any visible macro-cracking, resulted in the largest residual strengths with only a minimal loss of strength observed. However, the UXBX prestressed samples that did observe widespread macro-cracking had minimal residual strength (less than 10%).

Figure 14. Unconfined compressions results from all loading paths considered.

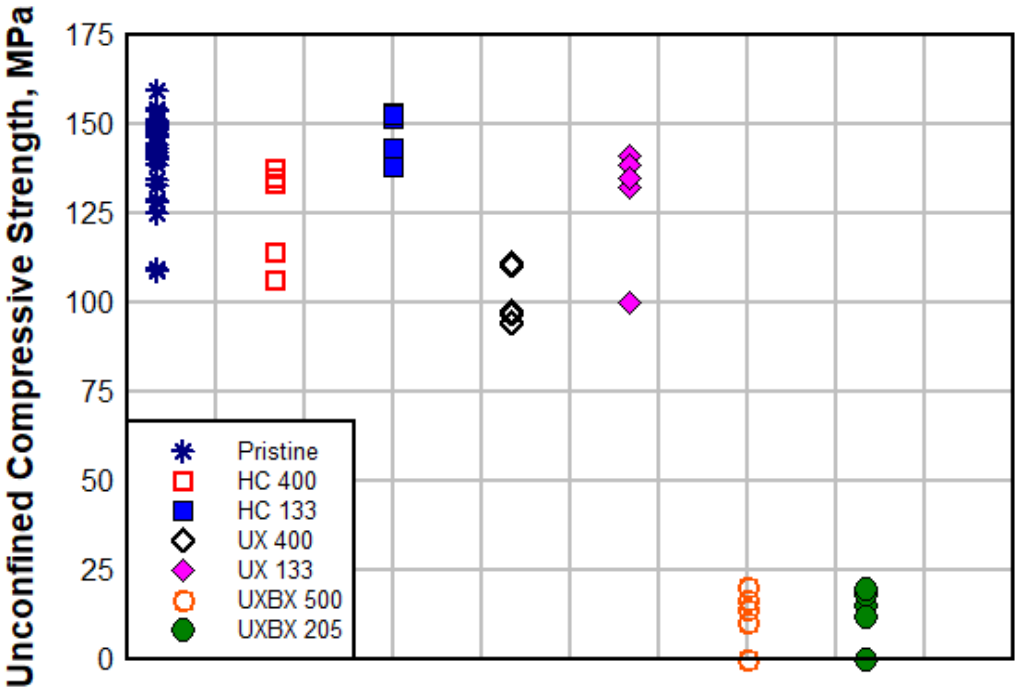

Table 3. Residual unconfined strength for HC, UX, and UXBX experiments.

Stress-Strain Path	Mean Normal Stress (MPa)	Residual Strength (%)
HC	400	89
HC	133	100
UX	400	72
UX	133	92
UXBX	500	9
UXBX	205	9

3 Model Comparisons with Experimental Data

3.1 Advanced Fundamental Concrete Model Description

The experimental data described herein was used to evaluate the Advanced Fundamental Concrete (AFC) constitutive material model (Adley et al. 2010). This model is widely used in hydrocodes by the DoD and has been previously used to successfully model penetration events (Adley et al. 2010; Sherburn et al. 2011; Sherburn et al. 2015; Chen et al. 1996). The AFC model relies on three principal components: (1) an equation of state for the pressure-volume relation that includes the nonlinear effects of compaction and locking, (2) a representation of the deviatoric strength of the intact and fully damaged material in the form of a pressure, strain rate, and three invariant-dependent yield limit surface, and (3) a pressure dependent scalar damage model that depends on both plastic volume and plastic shear strain. The damage evolution thereby includes processes like irreversible hydrostatic crushing, material yielding, and plastic flow. The model uses a linear constant shear modulus and fully decouples the hydrostatic and deviatoric responses.

3.2 Advanced Fundamental Concrete (AFC) Model Evaluation

Virtual experiments were conducted using the material model driver to replicate both the initial stress paths of HC, UX, and UXBX and the subsequent residual UC strength. The driver operates by a user-defined stress or strain boundary condition (mixed modes are possible). The boundary conditions are applied incrementally, both loading and unloading, with convergence towards stress equilibrium required for each successive load increment. The driver was specifically coded to allow for an upper loading limit to be set using the MNS boundary condition, which allowed for the virtual experiments to exactly match the peak loading from the actual experiments. Since the AFC material model is not stochastic in nature, only one virtual experiment was conducted for each prestress loading condition. The virtual experiments were conducted at a quasi-static strain rate of $10^{-5}\,s^{-1}$.

3.2.1 AFC Model Hydrostatic Compression Prestress Evaluation

The AFC material model driver was used to conduct virtual HC prestress experiments with HC loading and unloading up to peak MNS levels of 133 and 400 MPa. The model responses are plotted in Figure 15 in terms of MNS versus ε_{υ} and Figure 16 in terms of PSD versus MNS. Also plotted are the representative HC experimental stress-strain paths for comparison. The AFC HC loading follows the AFC pressure volume model for both pressure levels as expected. However, the AFC HC loading does not match the experimental data very well. This is due to the inability of the AFC model to produce shear-induced dilation, since the hydrostatic and deviatoric parts are fully decoupled. Thereby, as a practical matter, the model needs to be fit to either the HC or UX MNS-volumetric strain data, and typically, the UX experimental data are chosen, since this may be more representative of a penetration event.

Figure 15. Advanced Fundamental Concrete (AFC) model response data for HC tests at 133 and 400 MPa in terms of MNS versus ε_{υ}.

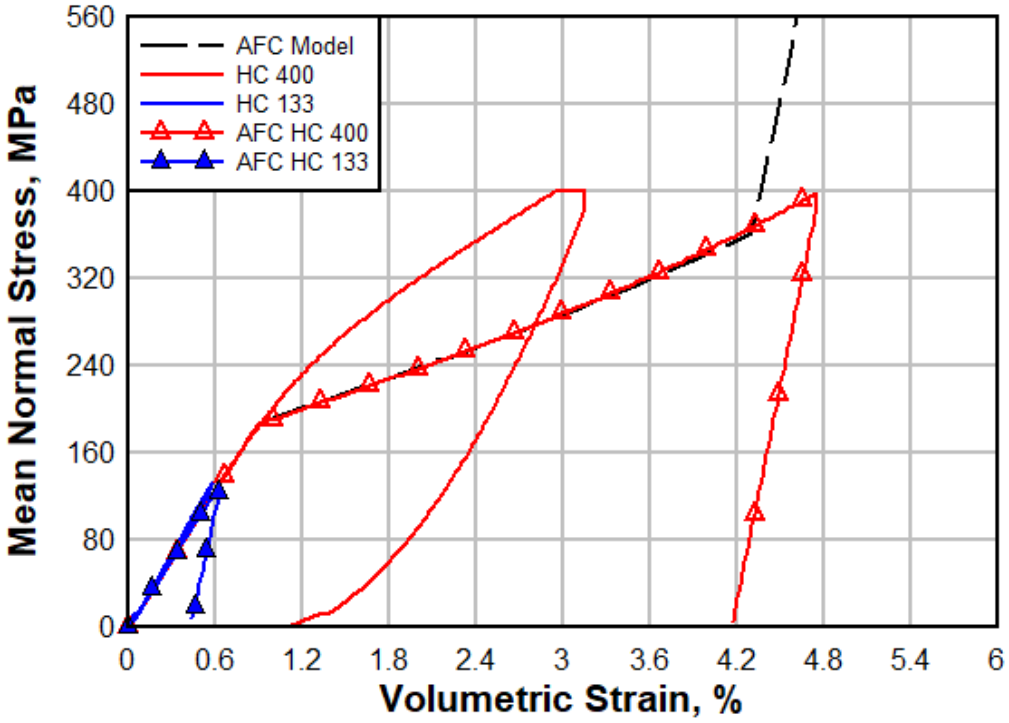

Figure 16. AFC model response data for HC tests at 133 and 400 MPa in terms of PSD versus MNS with peak TXC values.

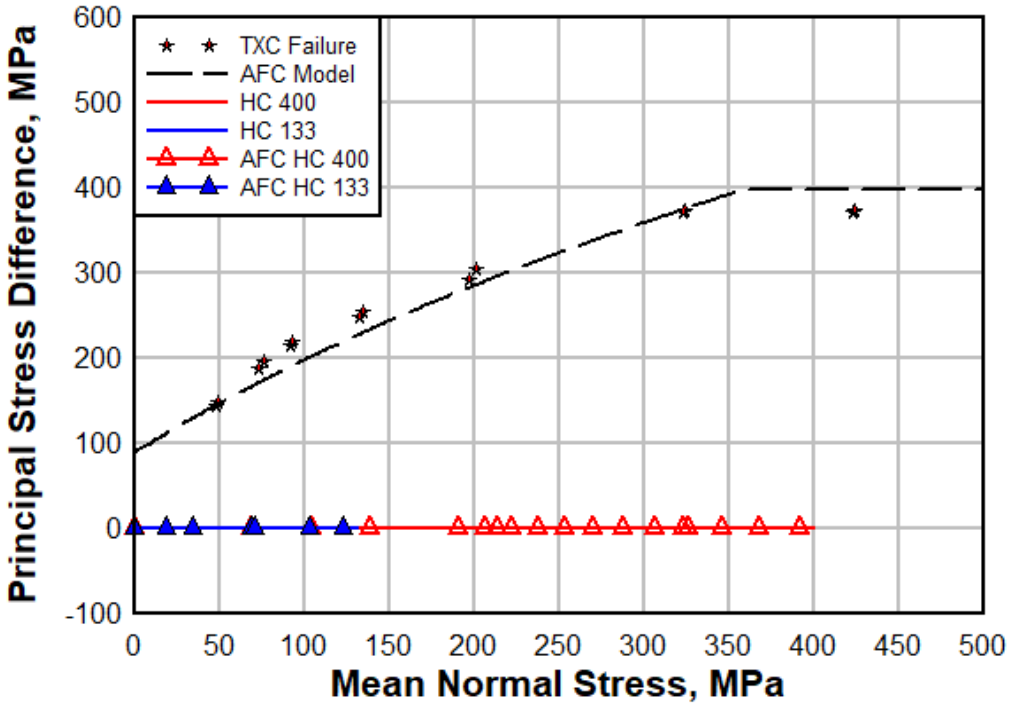

3.2.2 AFC Model Uniaxial Strain in Compression Prestress Evaluation

The AFC material model driver was used to conduct virtual UX prestress experiments with UX loading and unloading up to peak MNS levels of 133 and 400 MPa. The model responses are plotted in Figure 17 in terms of MNS versus ε_v and Figure 18 in terms of PSD versus MNS. Also plotted are the representative UX experimental stress-strain paths for comparison. The AFC UX loading follows the AFC pressure volume model for both pressure levels as expected. The AFC UX loading also matches the experimental data reasonably well, since the model was fitted using these data. However, in stress path space, the AFC UX does not match the experimental data in either loading or unloading. In fact, the AFC UX loading was shown to ride up the limit surface for MNS values greater than 200 MPa, unlike the experimental data that clearly lies well underneath the limit surface. This is due to the constant shear modulus used by the AFC model, which does not allow for the loading slope of the stress path (2G/K) to maintain the proper ratio.

The experimental data show that both the bulk modulus (Figure 17) and the shear modulus (Figure 4) soften with a greater softening observed for the shear modulus (Figure 18). For the AFC model however, for MNS values

greater than 200 MPa, the bulk modulus softens abruptly, but the shear modulus remains constant. Therefore, the AFC UX loading interacts with and rides up the limit surface. This can be resolved with a nonlinear softening shear modulus as opposed to the constant shear modulus currently used by the AFC model. Notice that this does not occur for the AFC UX loading up to 133 MPa, since this remains in the elastic range for the AFC model response.

Figure 17. AFC model response data for UX tests at 133 and 400 MPa in terms of MNS versus ε_v.

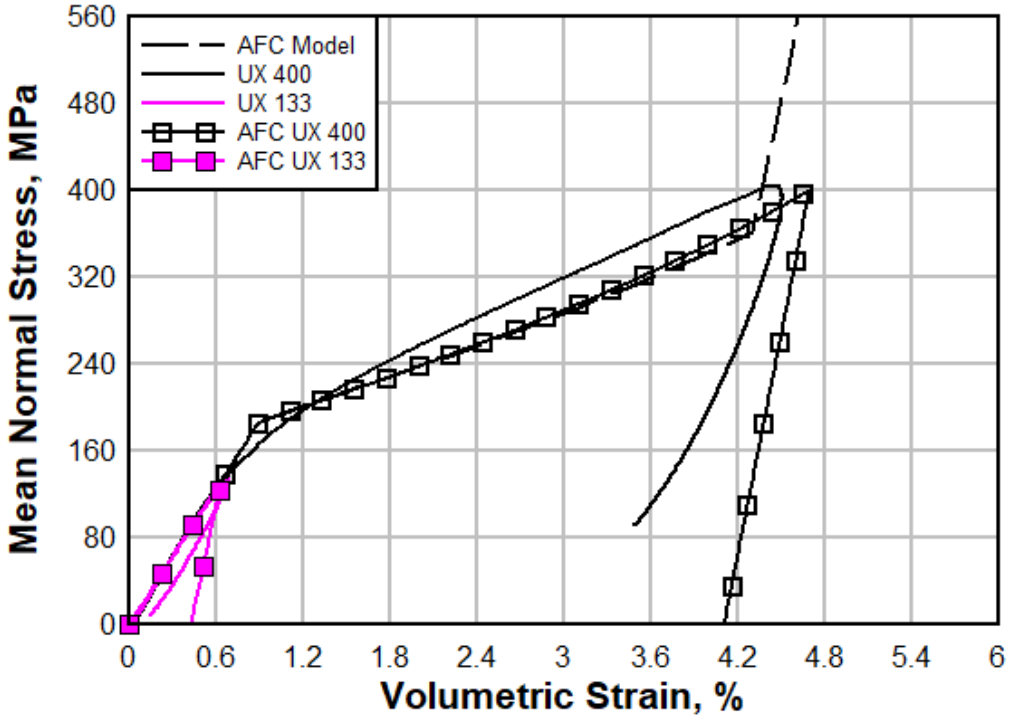

Figure 18. AFC model response data for UX tests at 133 and 400 MPa in terms of PSD versus MNS with peak TXC values.

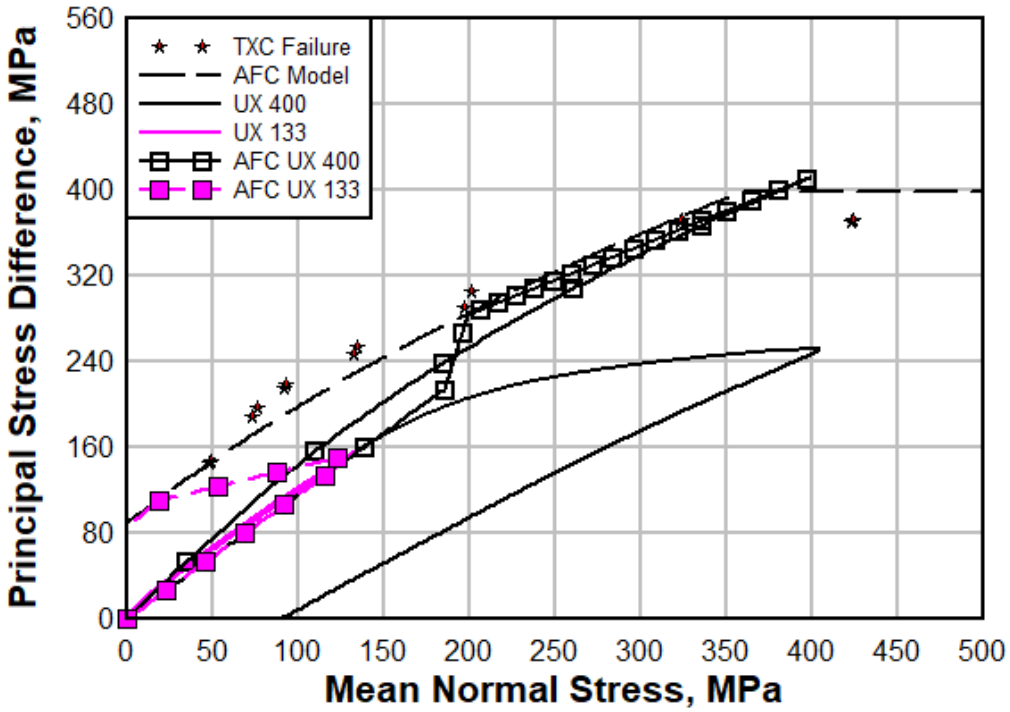

3.2.3 AFC Model Uniaxial Strain Load Biaxial Strain Unload Prestress Evaluation

The AFC material model driver was used to conduct virtual UXBX prestress experiments with UX loading and BX unloading up to peak MNS levels of 205 and 500 MPa. The model responses are plotted in Figure 19 in terms of MNS versus ε_v and in Figure 20 in terms of PSD versus MNS. Also plotted are the representative UXBX laboratory stress-strain paths for comparison. The material response from the AFC UXBX loading is similar to the response from the AFC UX loading with only minor exceptions, such as the peak MNS levels were different. The AFC BX unloading clearly engages with and follows the limits surface.

Figure 19. AFC model response data for UXBX tests at 205 and 500 MPa in terms of MNS versus ε_u.

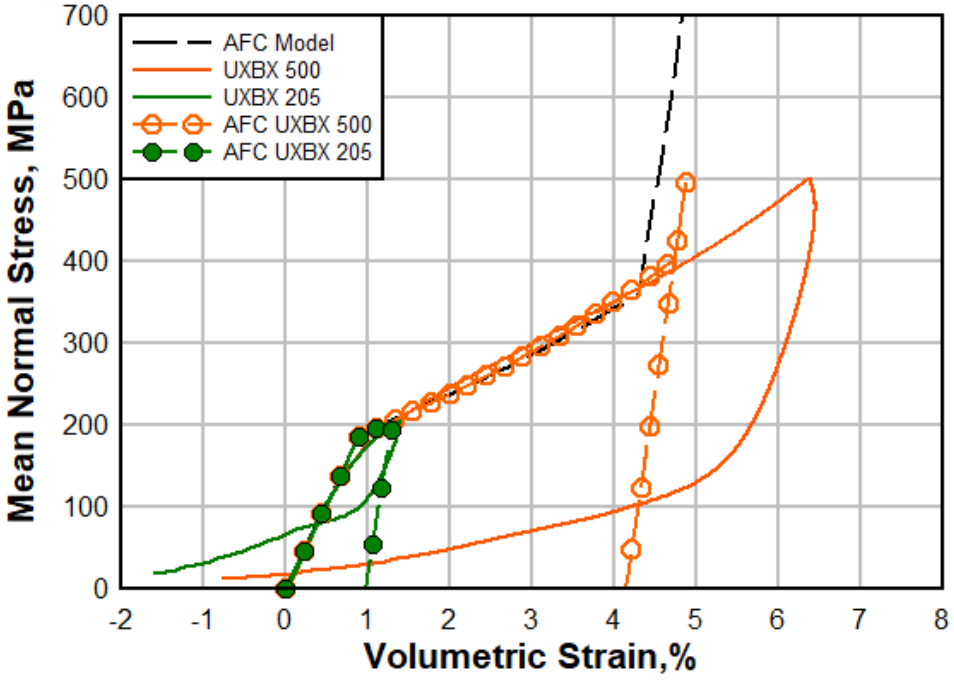

Figure 20. AFC model response data for UXBX tests at 205 and 500 MPa in terms of PSD versus MNS with peak TXC values.

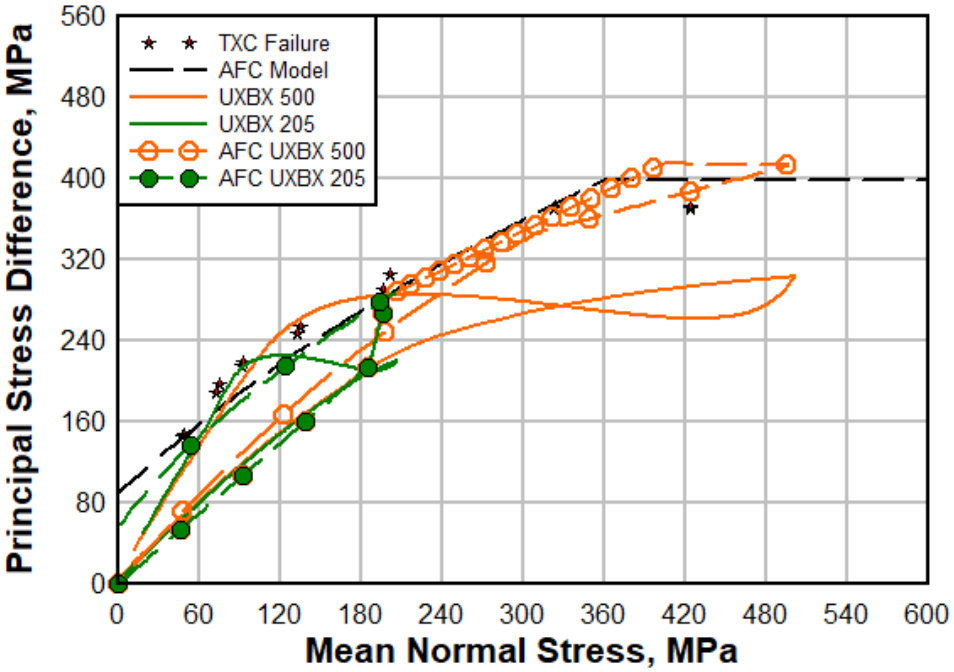

3.3 AFC Model Residual Strength Evaluation

To evaluate the individual stress paths with respect to their residual unconfined compressive strength, the AFC model driver was used to perform a pristine unconfined compressive virtual experiment resulting in a strength of 145 MPa. This value is slightly higher than the average value taken of the 30 pristine UC baseline experiments (141 MPa), since the AFC model was fit to the TXC experiment data. The AFC residual strength was similarly evaluated using a UC virtual experiment after each of the given prestress loading conditions were virtually conducted. The results for the residual UC strength evaluation of the AFC model are found in Table 4 and in Figure 21. The AFC model clearly underestimated residual strength and thus severely overestimated the material damage that was induced by each of the prestress conditions. Hence, there seems to be significant shortcomings in the AFC material model as fitted to the data presented herein.

Figure 21. Unconfined compressions results from all loading paths considered.

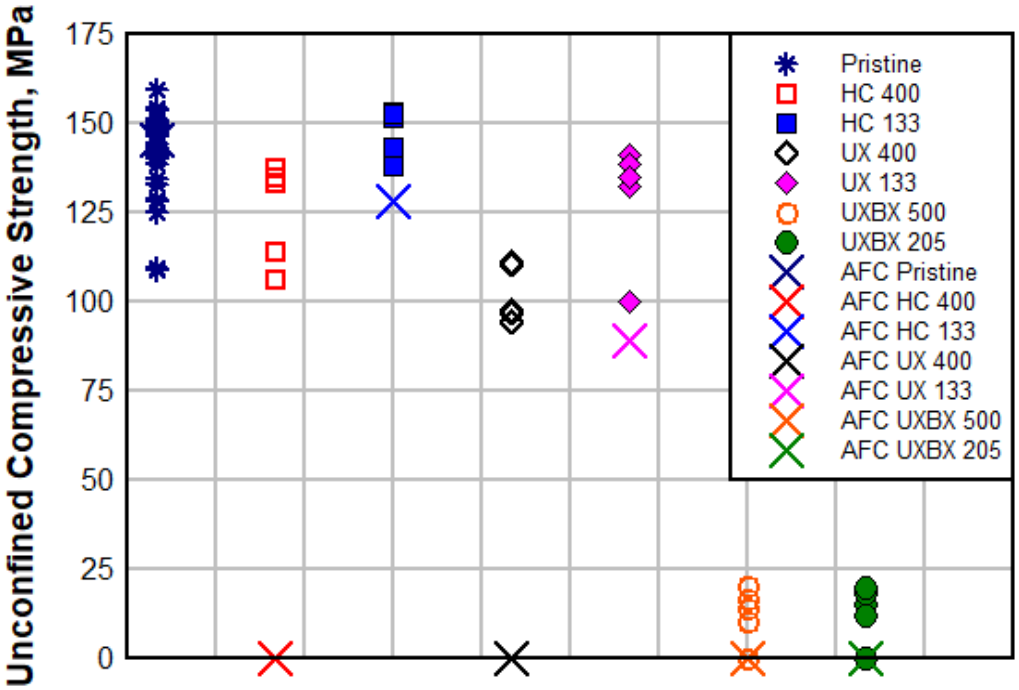

Table 4. Residual unconfined strength for HC, UX, and UXBX experiments with AFC model comparisons.

Stress-Strain Path	Mean Normal Stress (MPa)	Residual Strength, Experimental (%)	Residual Strength AFC Model (%)
HC	400	89	0
HC	133	100	88
UX	400	72	0
UX	133	92	61
UXBX	500	9	0
UXBX	205	9	0

4 Conclusions

Simplified mechanical loading paths—that may represent the more complex loading paths seen during penetration—were investigated using a triaxial chamber and a high-strength concrete. The objectives of this study were to determine the effects that the simplified stress-strain paths had on the material's unconfined residual strength. These paths included pure hydrostatic compression, uniaxial strain in compression, and uniaxial strain load biaxial strain unload. The stress-strain paths considered were conducted at low and high levels of confining pressure corresponding to quasi-brittle and ductile material responses. The low and high-pressure levels were selected based on results from simple triaxial compression experiments with constant radial pressure. X-ray micro-computed tomography analysis was used to investigate microstructure changes present within concrete specimens subjected to the simplified stress-strain paths. Results from the UX stress-strain path tests and the TXC experimental data were used to fit a widely used DoD model, which has been previously used successfully to model penetration events. A material model driver code was then used to conduct virtual experiments, which were intended to replicate the HC, UX, and UXBX stress-strain paths and their subsequent residual UC strength.

The experimental results indicated that the stress-strain paths associated with nonvisible micro-structural damage to the material were HC and UX, which tended to have a minimal impact on the residual UC compressive strength (less than 30%). While the stress-strain paths associated with visible macro-structural damage were UXBX, which had a significant effect on the residual UC compressive strength (greater than 90%). The results obtained from these virtual experiments revealed that the material model investigated had difficulties in matching the experimental data and consistently overestimated the material damage. The results obtained in this study can provide valuable insight for modifications of current concrete material models or contribute to the development of more robust, material-specific damage models for concrete.

The quantitative residual strength metric used in this study to determine the materials' residual strength—post an initial loading path—was unconfined compression, which investigates a quasi-brittle material response near the origin of the failure surface. In the future, it would be useful to perform a similar set of experiments in terms of loading path and pressures considered

but with a proposed alternative quantitative residual strength metric of high pressure triaxial compression. Using a high pressure triaxial compression residual strength metric would allow for investigation of material response near the upper portions of the experimental failure surface, where a ductile material response is typically observed. More specifically, do the conclusions of the current study remain valid if the confining pressure of the quantitative residual strength metric is increased?

References

Adley, M., A. O. Frank, K. T. Danielson, S. A. Akers, and J. L. O'Daniel. 2010. *The Advanced Fundamental Concrete (AFC) Model*. ERDC/GSL TR-10-51. Vicksburg, MS: US Army Engineer Research and Development Center, Geotechnical and Structures Lab. http://hdl.handle.net/11681/10480.

Akers, S. A., P. A. Reed, and J. Q. Ehrgott. 1986. *High-Pressure Uniaxial Strain and Triaxial Shear Test Equipment*. Vicksburg, MS: US Army Engineer Research and Development Center. https://apps.dtic.mil/sti/citations/ADA171877.

Balmer, G. G. 1949. *Shearing Strength of Concrete Under High Triaxial Stress: Computation of Mohr's Envelope as a Cure*. Technical Report No. SP-23. Denver, CO: Structure Research Laboratory.

Bazant, Z. P., F. C. Bishop, and T. P. Chang. 1986. "Confined Compression Tests of Cement Paste and Concrete Up to 300 Ksi." *ACI Journal* 33: 553–560. https://doi.org/10.14359/10448.

Bishop, A. W., and D. J. Henkel. 1957. "The Measurement of Soil Properties in the Triaxial Test." London: Edward Arnold. https://trid.trb.org/view/119099.

ASTM (American Society for Testing and Materials) International. 2018. *Standard Test Method for Compressive Strength of Cylindrical Concrete Specimens*. C39. West Conshohocken, PA: ASTM International.

ASTM (American Society for Testing and Materials) International. 2020. *Standard Test Method for Obtaining and Testing Drilled Cores and Sawed Beams of Concrete*. C42. West Conshohocken, PA: ASTM International. https://www.astm.org/c0039_c0039m-21.html.

ASTM (American Society for Testing and Materials) International. 2021. *Standard Specification for Flow Table for Use in Tests of Hydraulic Cement*. C230/C230M. West Conshohocken, PA: ASTM International. https://www.astm.org/c0230_c0230m-20.html.

Cement Suitability Initiative. 2009. "The Cement Sustainability Initiative." 1–42. http://docs.wbcsd.org/2009/06/CementIndustryEnergyAndCO2Performance.pdf.

Chen, J. S., C. Pan, C. T. Wu, W. K. Liu. 1996. "Reproducing Kernel Particle Methods for Large Deformation Analysis of Nonlinear Structures." *Computer Methods in Applied Mechanics Engineering* 139: 195–227. https://doi.org/10.1016/S0045-7825(96)01083-3.

Chuan-Zhi, W., G. Zhen-Hai, and Z. Xiu-Qin. 1987. "Experimental Investigation of Biaxial and Triaxial Compressive Concrete Strength." *ACI Materials Journal* 84: 92–100. https://doi.org/10.14359/1808.

Forquin, P., A. Arias, and R. Zaera. 2007. "An Experimental Method of Measuring the Confined Compression Strength of Geomaterials." *International Journal of Solids and Structures* 44: 4291–317. https://doi.org/10.1016/j.ijsolstr.2006.11.022.

Forquin, P., A. Arias, and R. Zaera. 2009. "Relationship Between Mesostructured, Mechanical Behavior and Damage of Cement Composites Under High-Pressure Confinement." *Experimental Mechanics* 49: 613–625. https://doi.org/10.1007/s11340-008-9172-y.

Forquin, P., and E. Piotroska. 2015. "Experimental Investigation of the Confined Behavior of Dry and Wet High-Strength Concrete: Quasi Static Versus Dynamic Loading." *Journal of Dynamic Behavior of Materials* 2015 (1): 191–200. https://doi.org/10.1007/s40870-015-0017-3.

Forrestal, M. J. 1985. "Penetration into Dry Porous Rock." *International Journal of Solids and Structures* 22: 1485–1500. https://doi.org/10.1016/0020-7683(86)90057-0.

Forrestal, M. J., B. S. Altman, J. D. Cargile and S. J. Hanchak. 1994. "An Empirical Equation for Penetration Depth of Ogive-Nose Projectiles into Concrete Targets." *International Journal of Impact Engineering* 15: 395–405. https://doi.org/10.1016/0734-743X(94)80024-4.

Frank, A. O. 2012. "An Elastic-Plastic Material Model for Concrete Under High Rate Impulsive Loads: Modeling, Implementation, and Testing of the High Rate Brittle (HRB) Concrete Model." ERDC/GSL TR-12-10. Vicksburg MS: US Army Engineer Research and Development Center, Geotechnical and Structures Lab. https://erdclibrary.on.worldcat.org/oclc/785589359.

Frank, A. O., M.D. Adley. 2011. "Improvements to the High-Rate-Brittle (HRB) Microplane Model: Linear Bounding Curves, Simplified Material Fitting and Model Evaluation." *82nd SAVIC Shock and Vibration Symposium*, Oct. 30–Nov. 3, Baltimore, MD.

Gabet, T., M. Yann, and L. Daudeville. 2007 "Triaxial Behavior of Concrete Under High Stresses: Influence of the Loading Path on Compaction and Limit States." *Cement and Concrete Research* 28: 403–412. https://doi.org/10.1016/j.cemconres.2007.09.029.

Gran, J. K., and D. J. Frew. 1996. "In-Target Radial Stress Measurements from Penetration Experiments into Concrete by Ogive-Nose Steel Projectiles." *International Journal of Impact Engineering* 19.8: 715–726. https://doi.org/10.1016/S0734-743X(97)00008-0.

Hanchak, S. J., M. J. Forrestal, E. R. Young and J. Q. Ehrgott. 1992. "Perforation of Concrete Slabs with 48 and 140 MPa Unconfined Compressive Strength." *International Journal of Impact Engineering* 121: 1–7. https://doi.org/10.1016/0734-743X(92)90282-X.

Holmquist, T. J., G. R. Johnson, and W. H. Cook. 1993. "A Computational Constitutive Model for Concrete Subjected to Large Strains, High Strain Rates, and High Pressures." In *Proceedings of the 14th International Symposium on Ballistics*, 26–29 September, Quebec City, Canada.

Imran, I., and S. J. Pantazopoulou. 1996. "Experimental Study of Plain Concrete Under Triaxial Stress." *ACI Materials Journal* 93 (6): 589–601. https://doi.org/10.14359/9865.

Johnson, G. R., R. A. Stryk, and S. R. Beissel. 2001. "User Instructions for the 2001 Version of the EPIC Code." Hopkins, MN: Alliant Techsystems, Inc.

Kolsky H. 1949. "An Investigation of the Mechanical Properties of Materials at Very High Rates of Loading." *Proceedings of the Physical Society* B62: 676–700. https://doi.org/10.1088/0370-1301/62/11/302.

Loeffler, C., Q. Ying, B. Martin, W. Heard, B. Williams, and X. Nie. 2018. "Detection and Segmentation of Mechanical Damage in Concrete with X-Ray Microtomography." *Materials Characterization* 142: 515–522. https://doi.org/10.1016/j.matchar.2018.06.018.

Lu, J., Lin, G., Z. Wang, and S. Xiao. 2003. "Reduction of Compressive Strength of Concrete Due to Triaxial Compressive Loading History." *Magazine of Concrete Research* 55: 34. https://doi.org/10.1680/macr.2004.56.3.139.

McGlaun, J.M., S. L. Thompson, and M.G. Elrick. 1990. "CTH: A Three-dimensional Shock Wave Physics Code." *International Journal of Impact Engineering* 10: 351–360. https://doi.org/10.1016/0734-743X(90)90071-3.

Mehta, P. K., and P. J. M. Monteiro. 2006. "Concrete Microstructure, Property, and Materials." Chicago: McGraw-Hill. https://www.worldcat.org/title/61254040.

Malecot, Y., X. H. Vu, and L. Daudeville. 2009. "Unconfined Compressive Strength is a Poor Indicator of the High-Pressure Mechanical Response of Concrete." *DYMAT* 2009: 1325–1331. https://doi.org/10.1051/dymat/2009187.

Nordendale, N. A., W. F. Heard, J. A. Sherburn, and P. K. Basu. 2015. "A Comparison of Finite Element Analysis to Smooth Particle Hydrodynamics for Application to Projectile Impact on Cementitious Material." *Computational Particle Mechanics* 3: 53–68. https://doi.org/10.1007/s40571-015-0092-1.

Ragalwar, K., Prieto, V., H. Fakhri, W. F. Heard, B. A. Williams, and R. Ranade. 2016. "Systematic Development of Environmentally Sustainable Ultra-High Performance Concrete." Kassel, Germany: HiPerMat. https://www.researchgate.net/publication/315805011_Systematic_Development_of_Environmentally_Sustainable_Ultra-High_Performance_Concrete.

Ragalwar, K. A., H. Nguyen, R. Ranade, W. F. Heard, and B. A. Williams. 2017. "Influence of Distribution Modulus of Particle Size Distribution on Rheological and Mechanical Properties of Ultra-High-Strength SHCC Matrix. *International Conference on Strain-Hardening Cement-Based Composites* 3: 221–229. https://doi.org/10.1007/978-94-024-1194-2_26.

Sfer, D., C. Ignacio, R. Gettu, and G. Etse. 2002. "Study of the Behavior of Concrete Under Triaxial Compression." *Journal of Engineering Mechanics* 128 (2): 156–163. https://doi.org/10.1061/(ASCE)0733-9399(2002)128:2(156).

Sherburn J. A., W. Heard, H. Park, and W. Chen. 2011. "Modeling of the Split Hopkinson Pressure Bar: Application to Cortuf." *82nd Shock and Vibration Symposium*, November, Baltimore, MD. https://www.researchgate.net/publication/268686411_Modeling_of_the_Split_Hopkinson_Pressure_Bar_Application_to_Cortuf.

Sherburn, J. A., M. J. Roth, J. S. Chen, and M. Hillman. 2015. "Meshfree Modeling of Concrete Slab Perforation Using a Reproducing Kernel Particle Impact and Penetration Formulation. *International Journal of Impact Engineering* 86: 96–110. https://doi.org/10.1016/j.ijimpeng.2015.07.009.

Vankirk, G., W. Heard, A. Frank, M. Hammons, and M. J. Roth. 2019. "Residual Structural Capacity of a High-Performance Concrete." *Dynamic Behavior of Materials* 1: 233–236. https://doi.org/10.1007/978-3-319-95089-1_42.

Vu, X. H., Y. Malecot, L. Daudeville, and E. Buzaud. 2008. "Experimental Analysis of Concrete Behavior Under High Confinement: Effect on Saturation Ratio." *International Journal of Solids and Structures* 46: 1105–1120. https://doi.org/10.1016/j.ijsolstr.2008.10.015.

Warren, T. L, A. F. Fossum, and D. J. Frew. 2004. "Penetration into Low Strength (23 MPa) Concrete: Target Characterization and Simulation." *International Journal of Impact Engineering* 30: 477–503. https://doi.org/10.1016/S0734-743X(03)00092-7.

White, M. P. 1946. "Effects of Impact and Explosion." Washington, DC: Office of Scientific Research and Development. https://apps.dtic.mil/sti/citations/AD0221586.

Williams, B. A., W. F. Heard, S. S. Graham, B. E. Martin, C. M. Loeffler, and X. Nie. 2019. "Mechanical Response and Damage Evolution of High-Strength Concrete Under Triaxial Loading." *Dynamic Behavior of Materials* 1: 69–71. https://doi.org/10.1007/978-3-319-95089-1_9.

Williams, E. M., S. A. Akers, and P. A. Reed. 2006. "Laboratory Characterization of SAM-35 Concrete." ERDC/GSL TR-06-15. Vicksburg, MS: US Army Engineer Research and Development Center, Geotechnical and Structures Lab. http://hdl.handle.net/11681/10388.

Williams, E. M., S. S. Graham, P. A. Reed, and T. S. Rushing. 2009. "Laboratory Characterization of Cor-Tuf Concrete With and Without Steel Fibers." ERDC/GSL TR-09-22. Vicksburg, MS: US Army Engineer Research and Development Center, Geotechnical and Structures Lab. http://hdl.handle.net/11681/10473.

Abbreviations

AFC	Advanced Fundamental Concrete
BX	Biaxial Strain
DoD	Department of Defense
ERDC	Engineer Research and Development Center
HC	Hydrostatic compression
HRB	High-Rate Brittle
HRWA	High-range water-reducing admixture
LVDT	Linear Variable Differential Transformer
micro-CT	Micro-Computed Tomography Imaging
MNS	Mean Normal Stress
PSD	Principal Stress Difference
TXC	Triaxial compression
UC	Unconfined compression
UX	Uniaxial strain in compression
UXBX	Uniaxial strain load biaxial strain unload
ε_a	Axial strain
ε_r	Radial strain
ε_v	Volumetric strain
σ_a	Axial stress
σ_r	Radial stress

REPORT DOCUMENTATION PAGE

1. REPORT DATE	2. REPORT TYPE	3. DATES COVERED	
		START DATE	END DATE
October 2023	Final Technical Report	FY20	FY21

4. TITLE AND SUBTITLE

Residual Strength of a High-Strength Concrete Subjected to Triaxial Prestress

5a. CONTRACT NUMBER	5b. GRANT NUMBER	5c. PROGRAM ELEMENT
		0602144A
5d. PROJECT NUMBER	**5e. TASK NUMBER**	**5f. WORK UNIT NUMBER**
BL9	SBL902	

6. AUTHOR(S)

George H. Vankirk, Andreas O. Frank, Michael J. Roth, Brett A. Williams, and William F. Heard

7. PERFORMING ORGANIZATION NAME(S) AND ADDRESS(ES)

US Army Engineer Research and Development Center (ERDC)
Geotechnical and Structures Laboratory (GSL)
3909 Halls Ferry Road
Vicksburg, MS 39180-6199

8. PERFORMING ORGANIZATION REPORT NUMBER

ERDC/GSL TR-23-18

9. SPONSORING/MONITORING AGENCY NAME(S) AND ADDRESS(ES)	10. SPONSOR/MONITOR'S ACRONYM(S)	11. SPONSOR/MONITOR'S REPORT NUMBER(S)
US Army Corps of Engineers (USACE) Washington, DC 20314-1000	USACE	

12. DISTRIBUTION/AVAILABILITY STATEMENT

Distribution Statement A. Approved for public release: distribution is unlimited.

13. SUPPLEMENTARY NOTES

14. ABSTRACT

This study investigates simplified mechanical loading paths that represent more complex loading paths observed during penetration using a triaxial chamber and a high-strength concrete. The objective was to determine the effects that stress-strain (load) paths have on the material's unconfined compressive (UC) residual strength. The loading paths included hydrostatic compression (HC), uniaxial strain in compression (UX), and uniaxial strain load biaxial strain unload (UXBX). The experiments indicated that the load paths associated with nonvisible microstructural damage were HC and UX—which produced minimal impact on the residual UC strength (less than 30%)—while the load path associated with visible macro-structural damage was UXBX, which significantly reduced the UC strength (greater than 90%). The simplified loading paths were also investigated using a material model driver code that was fitted to a widely used Department of Defense material model. Virtual experiment data revealed that the investigated material model overestimated material damage and produced poor results when compared to experimental data.

15. SUBJECT TERMS

Concrete; Constitutive Modeling; Mechanical Testing; Micro-CT; Penetration.

16. SECURITY CLASSIFICATION OF:			17. LIMITATION OF ABSTRACT	18. NUMBER OF PAGES
a. REPORT	b. ABSTRACT	C. THIS PAGE		
Unclassified	Unclassified	Unclassified	SAR	47

19a. NAME OF RESPONSIBLE PERSON	19b. TELEPHONE NUMBER (include area code)
George H. Vankirk	